Heliyon 10 (2024) e28066

Contents lists available at ScienceDirect

Heliyon

journal homepage: www.cell.com/heliyon

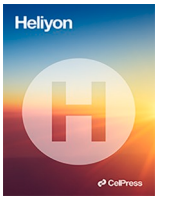

Research article

Synthesis, characterization, and efficacy evaluation of a PH-responsive Fe-MOF@GO composite drug delivery system for the treating colorectal cancer

Jia-Jie Shen [a,1], Shi-Jiao Xue [b,1], Zhang-Hao Mei [a], Ting-Ting Li [a], Hui-Fen Li [a], Xue-Fei Zhuang [a], Lin-Mei Pan [a,*]

[a] *Plant medicine Deep Processing Engineering Center, Nanjing University of Chinese Medicine, Nanjing, 210023, China*
[b] *Qidong Hospital of Traditional Chinese Medicine, Nantong, 226200, China*

ARTICLE INFO

Keywords:
Metal-organic framework
Graphene oxide
Luteolin
Matrine
Responsive release of acidic pH
Anti-colorectal cancer

ABSTRACT

Luteolin is a potent anti-colorectal cancer chemical. However, its effectiveness is hindered by its poor solubility in water and fat, and it is easy to degrade by gastrointestinal enzymes. In this study, a nano-composite carrier, NH_2-MIL-101(Fe)@GO (MG), based on aminated MIL-101(Fe) and graphene oxide (GO) was developed and evaluated. This carrier co-delivered luteolin and matrine, while marine was used to balance the pH for the nano-preparation. The loading capacities for luteolin and matrine were approximately 9.8% and 14.1%, respectively. Luteolin's release at pH = 5 was significantly higher than at pH = 7.4, indicating it had an acidic pH response release characteristic. Compared to MOF and GO alone, MG and NH2-MIL-101(Fe)@GO@Drugs (MGD) enhanced anti-cancer activity by inhibiting tumor cell migration, increasing ROS generation, and upregulating the expression of Caspase-3 and Caspase-9. In conclusion, this study contributes new ideas and methods to the treatment strategy of multi-component anti-colorectal cancer therapy. It also advances drug delivery systems and supports the development of more effective and targeted treatment approaches for colorectal cancer.

1. Introduction

Colorectal cancer, a malignancy of the digestive system, is the third most common and second deadliest cancer globally [1]. Traditional treatment options include surgery, radiotherapy, immunotherapy, and chemotherapy [2]. However, these methods often come with significant side effects and low survival rates [3–5]. Luteolin is an effective anti-colorectal cancer component [6,7]. However, luteolin's poor water and fat solubility, along with susceptibility to degradation by gastrointestinal enzymes, limit its oral bioavailability and clinical application [8,9]. To overcome these difficulties, modern nano preparation technology can be employed to synthesize a carrier which can effectively deliver luteolin and be suitable for the complex tumor microenvironment.

Metal-organic frameworks (MOFs) are a class of porous mixed organic-inorganic materials with unique properties, including a large specific surface area, adjustable pore size, easy synthesis, surface modifiability, and certain chemical instability [10,11]. MOFs have become as a research hotspot in the field of drug delivery platforms for tumor therapy. However, it is crucial not to overlook the

* Corresponding author.
E-mail address: linmeipan@njucm.edu.cn (L.-M. Pan).
[1] The authors contributed equally to this work.

https://doi.org/10.1016/j.heliyon.2024.e28066
Received 13 August 2023; Received in revised form 10 March 2024; Accepted 11 March 2024
Available online 15 March 2024

biocompatibility of MOFs, especially, the toxicity of metal ions and organic ligands within MOFs. Among the promising MOFs, iron-based MOFs stand out for their low toxicity, as iron is an essential trace element in the human body. Numerous studies have reported the utilization of iron-based MOFs like MIL-53, MIL-101, MIL-88, and MIL-100 for loading and delivering anticancer drugs, including curcumin [12], doxorubicin hydrochloride [13], 5-fluorouracil [14], aspirin [15], and camptothecin [16].

Graphene oxide (GO), a two-dimensional sp2-carbon nanomaterial, possesses several advantages, such as a large specific surface area, excellent electrical and thermal conductivity, and hydrophilicity [17]. The two-dimensional structure of GO provides numerous active sites for reacting with other functional groups through conjugation reactions or various other mechanisms [18,19]. Consequently, GO exhibits tremendous potential for biomedical applications, including drug delivery.

In this study, a novel drug delivery system consisting of MIL-101(Fe)@GO co-loaded with luteolin and matrine is built. The lamellar structure of GO is expected to be the in-situ growth point of MOF particles. The combination of MOF and GO, both possessing lamellar structures, not only enhances permeability and retention effects but also increases the uptake of drug. The system offers more effective drug binding sites and improves the hydrophilicity of the composite material [20–25]. Furthermore, it inhibits the aggregation and stacking of the two ingredients, resulting in a more uniform structure. Luteolin, a flavonoid compound, exhibits weak acidity, while the iron-based MOF demonstrates acid degradation properties. Consequently, matrine, another active anti-colorectal cancer drug [26], is selected to adjust the pH of the system, stabilize the carrier, and act as an excipient to enable the co-loading of both drugs.

2. Materials and methods

2.1. Reagents

N, N-dimethylformamide (DMF) and Luteolin were purchased from Aladdin Reagent Co., LTD (Shanghai, China). $FeCl_3{\cdot}6H_2O$ was obtained from Macklin Biochemical Technology Co., LTD (Shanghai, China). 2-amino-terephthalic acid was sourced from Sigma-Aldrich Pty Ltd (Darmstadt, Germany). GO was provided by Nanjing Jicang Nano Technology Co., LTD (Nanjing, China). Matrine was purchased from Nantong Feiyu Biotechnology Co., LTD (Nantong, China). RKO and FHC cells were provided by Jiangsu Collaborative Innovation Center for Traditional Chinese Medicine Prevention and Treatment of Tumor.

2.2. Samples preparation

The final preparation method was determined based on the investigation of the several factors, including the amount of DMF, the reaction materials ratio, the amount of GO, the reaction time, and temperature (Supplementary figs. 1–10; Supplementary tables 1–4).

NH_2-MIL-101(Fe)@GO (MG): $FeCl_3{\cdot}6H_2O$ (1.461 g), 2-amino-terephthalic acid (438.3 mg), GO (73.05 mg) was dispersed in DMF (30 mL). After mixing and stirring for 30 min, the mixture was transferred to a Teflon reactor and reacted in an oven at 110 °C for 24 h. After cooling, the obtained solution was centrifuged at 5000 rpm for 10 min, followed by 3 washes with DMF and ethanol. Finally, the sediment was activated in the oven at 110 °C for 24 h to obtain the MG.

NH_2-MIL-101(Fe)@GO@Luteolin@Matrine (MGD): Equal amounts of luteolin, matrine, and MG were dispersed in an appropriate amount of anhydrous ethanol and stirred at room temperature for 6 h to achieve full contact between the drug and the carrier. The solution was centrifuged at 5000 rpm for 10 min, and the precipitate was washed with anhydrous ethanol to remove the free drug. The product was dried in a low-temperature oven to obtain MGD. HPLC was used to detect the loading capacity of the drug, calculated as follows (the HPLC conditions was shown in supplementary materials):

$$\text{Luteolin loading } (\%\text{w}) = \frac{\text{Total amount of luteolin} - \text{Free amount of luteolin}}{\textit{Mass of carrier}} \times 100$$

$$\text{Matrine loading } (\%\text{w}) = \frac{\text{Total amount of } \textit{Matrine} - \text{Free amount of } \textit{Matrine}}{\textit{Mass of carrier}} \times 100$$

2.3. Structural characterization

A variety of structural characterizations were conducted, including scanning electron microscope (SEM) image, transmission electron microscope (TEM) image, X-ray diffraction (XRD), Brunauer-Emmett-Teller (BET) test, X-ray photoelectron spectroscopy (XPS) analysis, particle size (PS), surface zeta potential (SZP), and thermal gravity analysis (TGA). These were performed to confirm the successful synthesis of the carrier materials and the effective loading of the drugs, as well as study their physicochemical properties.

SEM: The GeminiSEM300 field emission SEM (FE-SEM) (Zeiss, Germany) was used to examine the morphology and elemental distribution.

TEM: A Tecnai F20 TEM (FEI, USA), operated at an accelerated voltage of 200 kV, was used to observe the particle structure at a higher resolution.

XRD: XRD patterns were collected using a D8 Advance X-ray diffractometer (Bruker, Germany), with Cu Kα radiation (wavelength 1.5418 Å), scanning in the range of 5–90° (scanning step size: 0.02°, scanning speed: 10°/min, working voltage: 40 kV, working current: 30 mA).

BET: BET tests were carried out using an ASAP2420 automatic specific surface area and pore analyzer (Micromeritics, USA), with a degassing temperature of 110 °C and a degassing time of 12 h. BET and Barrett-Joyner-Halenda (BJH) methods were used to calculate

the BET specific surface area, pore volume, and pore diameter, respectively. Since the MGD system contained matrine with a low melting point, BET detection was only performed on MG.

XPS: A Nexsa X-ray photoelectron spectrometer (Thermo Fisher, GBR) was used to study the composition and elemental binding modes in the materials. The analysis chamber was maintained at a vacuum level of 5×10^{-10} Pa, and Al Kα rays (hv = 1486.68 eV) were used as the excitation source at a working voltage of 15 kV and a filament current of 10 mA. The signal was accumulated 5–10 times, and the energy standard for C1s = 284.80 eV was used for data calibration.

PS and SZP: PS and SZP were measured using a ZS90 nanoparticle size potential analyzer (Malvern, GBR). Fourier Transform infrared spectroscopy (FT-IR) spectra were obtained using a Nicolet iS5 Fourier Transform infrared spectrometer (Thermo Fisher, GBR), covering the spectral range of 500–4000 cm^{-1}.

TGA: A thermogravimetric analyzer (Mettler, Germany) was used to investigate the thermal stability of the materials in a temperature range of 30–800 °C with a 30 °C/min heating rate.

2.4. In vitro drug release studies

The *in vitro* diffusion method was used to study the regularity of drug release. Specifically, MGD (30 mg) was introduced to 1% Tween-80 PBS buffer solution (30 mL) at pH value of 5 and 7.4, with stirring at 37 °C using a magnetic stirrer. At specific time intervals (025, 0.5, 1, 2, 3, 4, 5, 6, 7, 8, 9, 10, 11, 12, 24, 48, and 72 h), 1 mL of the solution was taken to determine the drug solubility, and 1 mL of fresh buffer solution was added to maintain a constant volume. HPLC was utilized for evaluating the drug release. The subsequent formulas were employed to calculate and plot the cumulative *in vitro* release curve (n = 3).

$$W\% = \frac{C_n V_n + \sum_{0}^{i} C_i V_i}{M} \times 100$$

$C_{n/i}$ (mg/mL) referred to the drug concentration at the *n/i* time point; V_n (mL) denoted the total system volume (30 mL); V_i (mL) stand for the sample volume at the *i*-time point; M (mg) represented the total mass of drug; and W denoted the percentage of cumulative release.

2.5. Cytotoxicity assay

Cell viability was measured using the CCK-8 method. RKO and FHC cells were seeded into 96-well plates and incubated at 37 °C in 5% carbon dioxide for 12 h. The cells were then treated with NH_2-MIL-101(Fe), GO, MG, and MGD at varying concentrations (0, 3.125, 6.25, 12.5, 25, 50, 100, 200 μg/mL) for 24 h. The supernatant was discarded, and the cells were washed with PBS to remove unabsorbed drugs. A solution containing 10% CCK-8 reagent (100 μL) was added to each well and incubated for 2–3 h. Cell survival rate was calculated based on the absorbance at 450 nm.

2.6. Wound healing assay

RKO cells were inoculated into a six-well plate and incubated for 12 h. The back of the plate was marked to divide each well into three sections. After washing each well 3 times with PBS to remove detached cells, the initial scratch was recorded using an inverted microscope (Zeiss, Germany). MG and MGD (100 μg/mL) were added to the wells, and photographs were captured at 24 h and 48 h post-treatment to document the scratch status at the same position.

2.7. ROS releasing assay

RKO cells were seeded into 6-well plates and incubated for 12 h. The cells were then treated with MG and MGD (100 μg/mL) for 24 h. After washing the cells three times with PBS to remove free drugs, the cells were digested and collected using pancreatic enzymes. DCFH-DA (10 μM) was added to the cells and incubated for 20 min, with the mixture being inverted and mixed every 5 min to ensure full probe-cell contact. The cells were then washed three times with FBS-free cell culture solution to remove any DCFH-DA that did not enter the cells. Fluorescence intensity was measured using a fluorescent enzyme labeling instrument (Tecan, Swiss). The above steps were without cell digestion, allowing the probe to directly contact the adherent cells. The ROS fluorescence intensity was directly observed using an inverted fluorescence microscope (Nikon, Japan).

2.8. Effects on protein expression of caspase-3 and caspase-9

The cell culture procedure was repeated until the RKO cells reached the appropriate state. The cells were then treated with 100 μg/mL of MG and MGD for 24 h. After collection, the cells were lysed to extract intracellular proteins. Western blotting was performed to detect changes in the expression of caspase-3 and caspase-9.

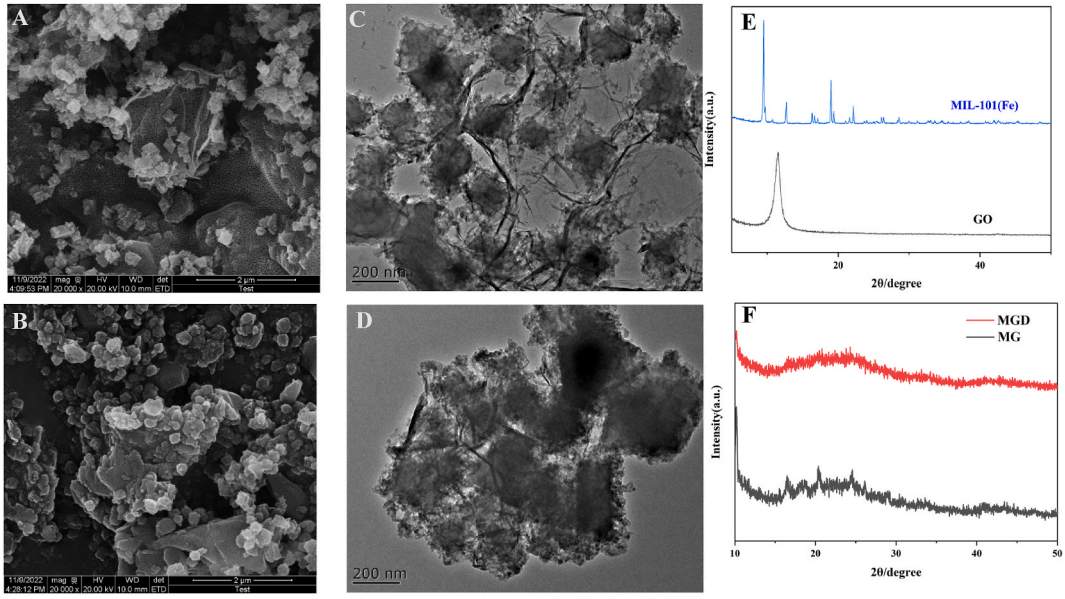

Fig. 1. Synthesis and characterization. A, SEM images of MG; B, SEM images of MGD; C, TEM images of MG; D, TEM images of MGD; E, XRD pattern of MIL-101(Fe) and GO; F, XRD pattern of MG and MGD.

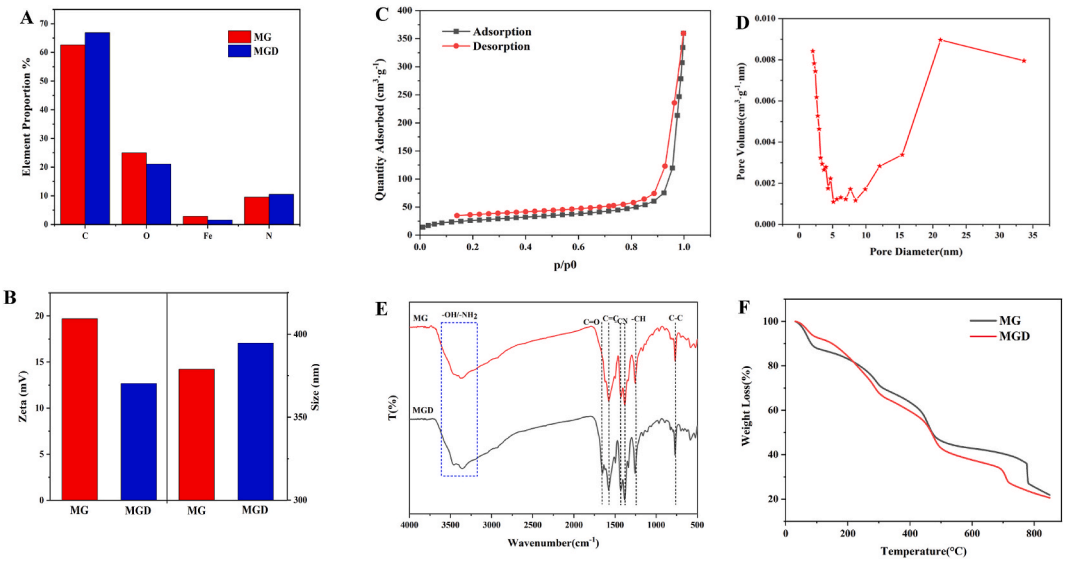

Fig. 2. Characteristics. A, Elemental proportion; B, SZP and PZ; C, Nitrogen adsorption and desorption isotherms of MG; D, Pore size distribution of MG; E, FT-IR; F, TGA.

3. Results and discussion

3.1. Synthesis and characterization of MG and MGD

MG was synthesized using a solvothermal method. In this process, GO with two-dimensional lamellae served as the *in-situ* growth point for MOF particles, which included the metal center, organic ligand, and solvent. Under high temperature, the MOF particles were synthesized and uniformly dispersed on the surface of GO, resulting in the formation of the MG.

To load the drug, luteolin, matrine and carrier materials were stirred together. As shown in Fig. 1A and C, the iron-based MOFs exhibited an octahedral pyramid morphology dispersed on the surface of the GO lamellae. However, after drug loading, the MOF structure transformed into an irregular polyhedral form, and the GO lamellae thickened (Fig. 1B and D). Obvious absorption peaks were observed around 9.84°, 16.36°, 20.4°, and 24.6° (Fig. 1F), consistent with reference [27]. In addition, compared to MOF and GO

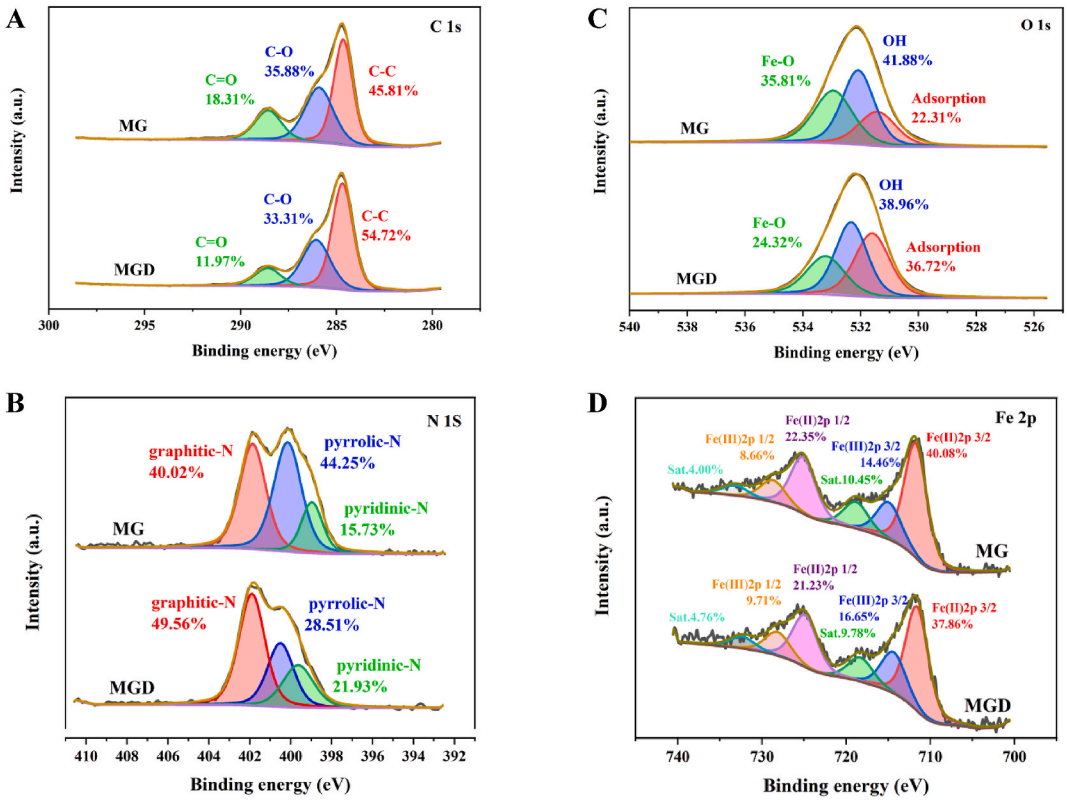

Fig. 3. XPS diagrams of MG and MGD.

alone (Fig. 1E), the positions of characteristic peaks corresponded to each other, indicating the successful synthesis of MG. However, the addition of GO and drugs led to a reduction in characteristic peak intensity, likely attributed to X-ray diffraction reduction.

The BET test results revealed that the specific surface area of MG was approximately 90.36 cm^3/g, and the pore size was around 2.38 nm, indicating its classification as a mesoporous material (Fig. 2C and D). It was evident that MG and MGD predominantly consist of four elements: C, O, Fe, and N (Supplementary figs. 11A–D). Upon drug loading, there were changes in the element proportions, with an increased proportion of C and N elements and a decreased proportion of O and Fe elements (Fig. 2A). The SZP and PS of MG and MGD were also measured, showing an increase in PS from 378.9 nm to 394.6 nm and a decrease in SZP from 19.7 mV to 12.7 mV after drug loading (Fig. 2B).

To further confirm the drug loading, FT-IR measurements were performed. The results illustrated wide absorption bands in the range of 3200–3600 cm^{-1}, attributed to stretching vibrations of hydroxyl (-OH) and amino (-NH_2) groups (Fig. 2E). The characteristic peak observed at 1613 cm^{-1} corresponds to the stretching vibration of the C═O bond in the carboxyl group [28]. The peak at 1578 cm^{-1} represented stretching vibrations of the C═C unsaturated bond in the carbon skeleton. The two peaks 1437 and 1350 cm^{-1} were attributed to the stretching vibration bonds for the C–N bonds in amide moieties [29]. The peaks near 1250 and 770 cm^{-1} corresponded to the stretching vibrations of –CH and C–C, respectively. Notably, the absorption peak strength of the wide absorption band near 3200–3600 cm^{-1} slightly weakened after loading luteolin, potentially due to the formation of complex bonds between the hydroxyl groups of luteolin and the central iron of the MOF. This weakening could result in decreased resonance strength of hydroxyl and amino groups on the composite carrier's surface. Moreover, the strength of the characteristic peak at 1613 cm^{-1} corresponding to the C═O bond significantly decreased after drug loading, possibly due to hydrogen bonding between luteolin and the oxygen-containing functional groups on the GO surface.

TGA demonstrated both MG and MGD had an excellent thermal stability (Fig. 2F). In the C1s spectrum of MG, three peaks were observed at 284.5, 286.3, and 287.7 eV, corresponding to C–C, C–O, and C═O, respectively [30]. The O1s spectrum exhibited peaks at 532 and 533 eV, representing the –OH and Fe–O bonds in the sample, while peaks around 531.5 eV could be attributed to oxygen absorption [31]. In the N1s spectrum, the three main peaks observed at 398.2, 400.5, and 401.9 eV corresponded to pyridine-N, pyrrole-N, and graphite-N, respectively. The proportion of nitrogen in the system was relatively low, possibly due to the high reaction temperature leading to the partial destruction of C–N bonds [32]. In the Fe2p spectrum, the two main peaks at 711 and 725.1 eV corresponded to Fe2p3/2 and Fe2p1/2, respectively, indicating the presence of both Fe^{2+} and Fe^{3+} in the composite [33].

After drug loading, there were significant changes in the proportions of binding modes for each element (Fig. 3A–D). The proportion of C═O and Fe–O decreased from 18.31% to 11.97%, and from 35.81% to 24.32%, possibly due to the successful loading of luteolin. While, the changes in the N1s spectrum could be attributed to the addition of matrine.

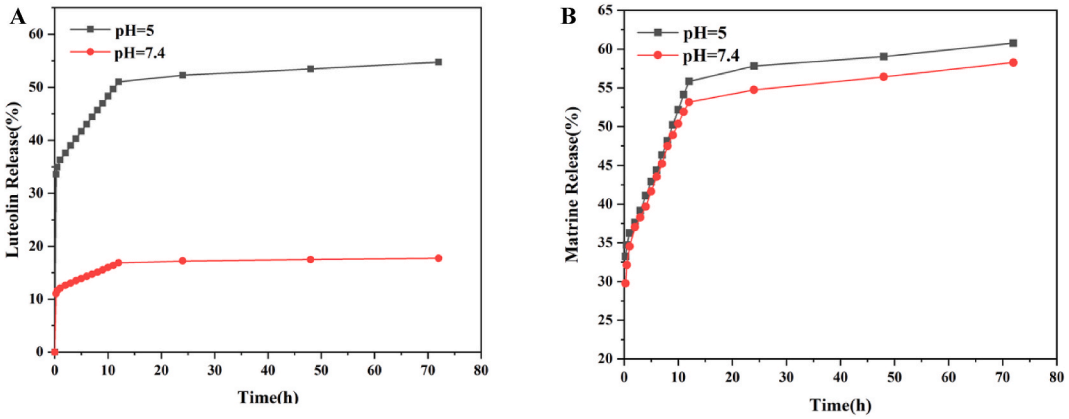

Fig. 4. Cumulative release curves of drugs. A, Luteolin; B, Matrine.

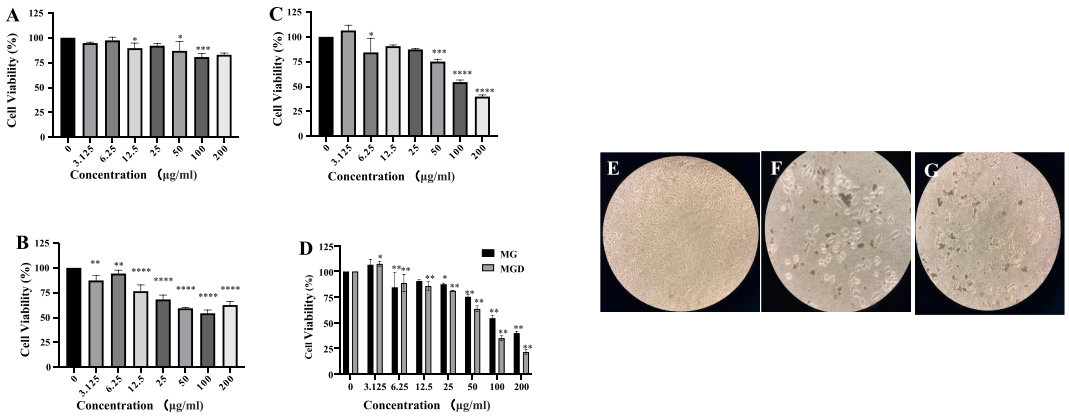

Fig. 5. Effects of different drugs on RKO cell viability. A, Effect of NH2-MIL-101(Fe) on RKO cell viability; B, Effect of GO on RKO cell viability; C, Effect of MG on RKO cell viability; D, Effect of MG and MGD on RKO cell viability; E, Blank RKO cells morphology; F, Morphology of RKO cells at 0 h of administration (MGD); G, Morphology of RKO cells at 24 h of administration (MGD).

The characterizations not only offered physical parameters of MG and MGD but also confirmed the successful synthesis of the carrier and provided evidence of the success for drug loading.

3.2. *Drug loading and release*

Luteolin and matrine, which belonged to flavonoids and alkaloids respectively, were loaded onto the carrier using the following mechanism: the o-phenol hydroxyl group of luteolin could form a complex with iron ion in the metal center, and this complex bond could be broken under the influence of acidic H^+. Moreover, the presence of H^+ leaded to the gradual collapse of the MOF skeleton, facilitating drug release [16,34]. Additionally, due to the inclusion of GO, the numerous oxygen-containing functional groups on its surface could interact with the phenolic hydroxyl group of luteolin through hydrogen bonding. The π-π stacking between benzene rings also contributed to the loading of luteolin. On the other hand, matrine, being positively charged, could be electrostatically attracted to the negatively charged GO surface, resulting in successful drug loading.

The theoretical loading capacity of the two drugs were determined by HPLC, which was about 9.8% and 14.1% for luteolin and matrine, respectively. The drug release experiment of MGD was conducted by an *in vitro* diffusion method. Under acidic conditions (pH = 5), the release of luteolin was significantly higher than that under neutral conditions(pH = 7.4), while the release of matrine showed no correlation with pH conditions. Both drugs exhibited an initial sudden release, followed by gradual slow release. At the end of the 72-h experiment, the combined drug loading system released approximately 54.8% of luteolin and 60.8% of matrine at pH 5, whereas only 17.8% of luteolin and 58.3% of matrine were released at pH 7.4 (Fig. 4A and B), suggesting that MGD had the potential to release luteolin under acidic conditions.

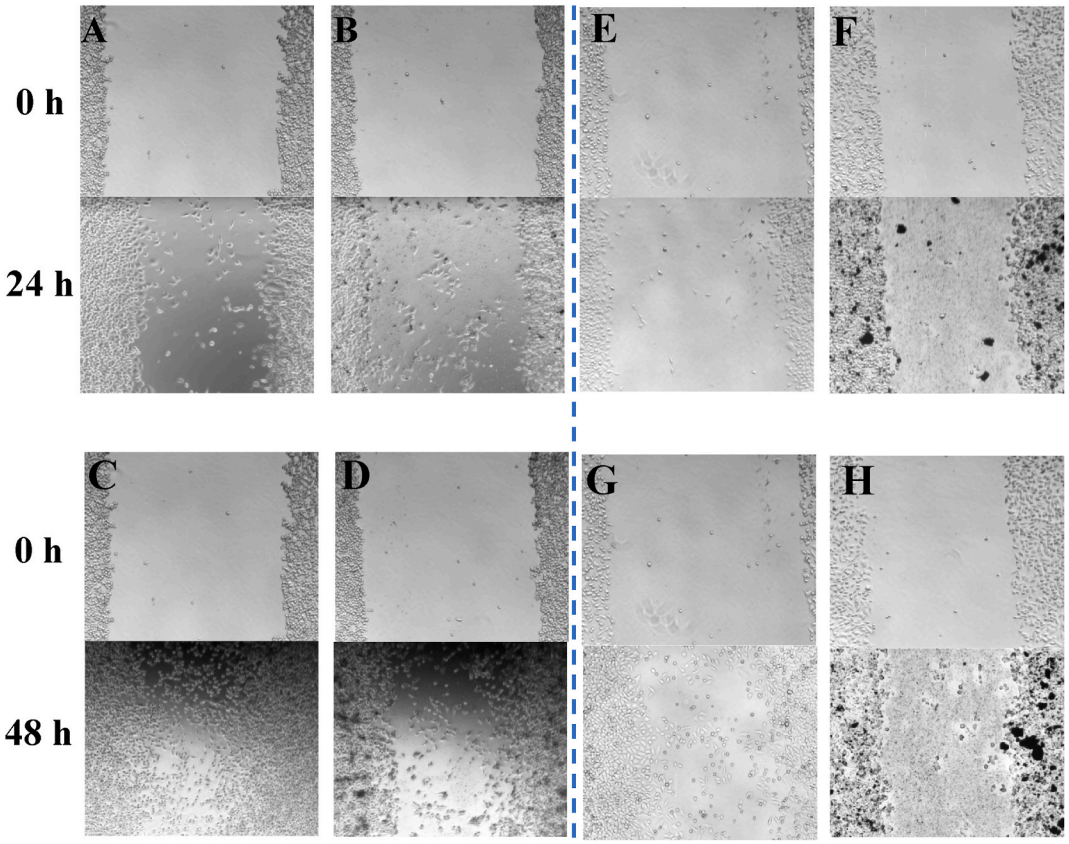

Fig. 6. Effects of MG and MGD on RKO cells migration. A-D, MG group; E-H, MGD group. (A,C,E, and G are blank RKO cells without drug effect).

3.3. Efficacy evaluation in vitro

3.3.1. Cell cytotoxicity assay

The PS results of MGD suggested its potential to increase accumulation at the tumor site by enhancing the permeability and retention effect (EPR) [35]. Additionally, the positive charge on the surface of MGD allowed it to better interact with the negatively charged surface of tumor cells, enhancing its potential to enter the interior of cells.

Normal RKO cells exhibited irregular spindle-shaped morphology (Fig. 5E). At 0 h, evident MGD particles were observed (Fig. 5F), while at 24 h, significant drug adsorption around RKO cells was visible, coinciding with a noticeable reduction in the number of RKO cells (Fig. 5G). Subsequently, the CCK-8 method was used to investigate the effects of NH2-MIL-101(Fe), GO, MG, and MGD on RKO activity in colorectal cancer cells (Fig. 5A–D). NH2-MIL-101(Fe) did not significantly inhibit RKO cell viability at various concentrations, while the effect of GO on RKO cell viability was concentration-dependent. Overall, as the concentration increased, the inhibitory effect slightly strengthened. MG exhibited significantly inhibitory effects on RKO cells, particularly at medium and high concentrations (25–200 μg/mL), where the inhibitory effect was notably higher than that of either component alone at the same concentration. Furthermore, MGD with luteolin and matrine demonstrated further enhancement in comparison to the blank composite carrier. These results indicated that the composite vector held a considerable advantage over MOF and GO alone, and combining the vector with the drugs could further amplify this advantage. In addition, the effects of MGD on the viability of RKO and FHC cells were also conducted to preliminarily evaluate the *in vivo* safety of MGD. The results showed that MGD did not affect the normal proliferation of FHC cells at low to medium concentration, but had a weak inhibitory effect at high concentration, which may be related to the increase of GO content (Supplementary fig. 12).

3.3.2. Cell migration assay

Both luteolin and matrine have been reported to exhibit inhibitory effects on tumor cell migration [36–39] Thus, the effects of MG and MGD on RKO cell migration were investigated (Fig. 6). In the control group, RKO cells migrated towards the center after 24 h (Fig. 6A and E), and nearly all RKO cells occupied the middle blank area after 48 h(Fig. 6C and G). At 24 h and 48 h after MG administration, there was also a substantial increase in scratch center cells, indicating that MG did not significantly inhibit RKO cell migration(Fig. 6B and D). However, after 24 h of MGD administration, RKO cells exhibited minimal migration(Fig. 6F), and there was no significant migration even after 48 h(Fig. 6H). Hence, MGD demonstrated a significant inhibitory effect on the migration of RKO

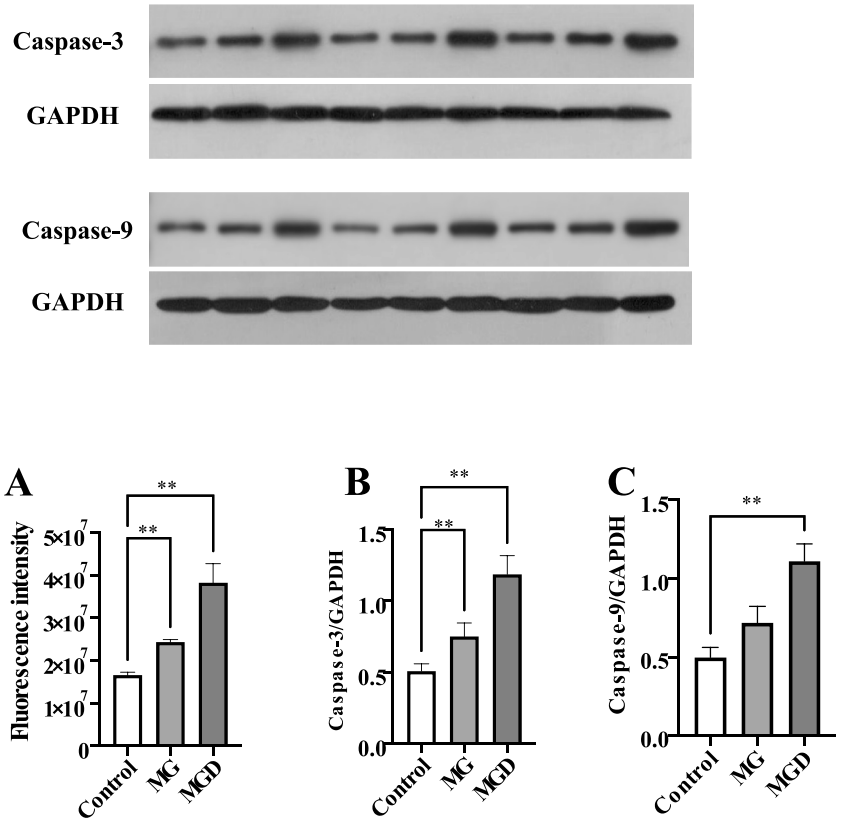

Fig. 7. Effects of MG and MGD on ROS and apoptosis factor. A, ROS; B, Caspase-3; C, Caspase-9.

cells when compared with MG.

3.3.3. ROS and apoptosis factor detection

Numerous studies have validated the anti-tumor role of iron-based MOF through the Fenton reaction [40,41]. Upon uptake by tumor cells, nanomaterials containing iron-based MOF release iron ions within intracellular lysosomes, which could induce tumor cell apoptosis by promoting ROS generation. Additionally, the Caspase family proteases played a crucial role in apoptotic pathways [42–45]. Consequently, the changes in ROS, Caspase-3, and Caspase-9 contents in RKO cells were concurrently assessed after treatment with MG and MGD. The results indicated that, compared to MG, MGD could further enhance ROS production in cells and up-regulate the expression of Caspase-3, and Caspase-9 (Fig. 7A–C).

4. Conclusion

This study successfully synthesized a complex carrier based on NH2-MIL-101(Fe) and GO with uniform particle size and a stable structure. The carrier efficiently loaded both luteolin and matrine, resulting in a complex drug delivery system capable of releasing luteolin in response to acidic pH. *In vitro* pharmacodynamic experiments demonstrated a synergistic effect between NH2-MIL-101(Fe) and GO. GO could enhance the composite vector's anti-colorectal cancer effect. This system effectively inhibited the proliferation and migration of RKO cells by increasing ROS release and up-regulating of Caspase-3, and Caspase-9. This work exhibited the advantages of combining MOF and GO, demonstrating the potential of MOF@GO drug delivery systems in drug loading and anti-tumor applications. This approach provides new ideas and methods for the treatment strategy of colorectal cancer by multi-component.

Data availability statement

The data that support the findings of this study are available on request from the corresponding author. The data are not publicly available due to privacy or ethical restrictions.

CRediT authorship contribution statement

Jia-Jie Shen: Writing – original draft, Data curation, Conceptualization. **Shi-Jiao Xue:** Writing – original draft, Methodology, Data

curation. **Zhang-Hao Mei:** Visualization, Formal analysis. **Ting-Ting Li:** Visualization, Formal analysis. **Hui-Fen Li:** Software, Resources. **Xue-Fei Zhuang:** Software, Resources. **Lin-Mei Pan:** Writing – review & editing, Supervision, Conceptualization.

Declaration of competing interest

The authors declare that they have no known competing financial interests or personal relationships that could have appeared to influence the work reported in this paper.

Acknowledgments

This research was supported by the national key research and development program of China (2017YFC1700602).

Appendix A. Supplementary data

Supplementary data to this article can be found online at https://doi.org/10.1016/j.heliyon.2024.e28066.

References

[1] Y. Xi, P. Xu, Global colorectal cancer burden in 2020 and projections to 2040, Transl Oncol 14 (2021) 101174.
[2] L. Ruiz-Lopez, I. Blancas, J.M. Garrido, N. Mut-Salud, M. Moya-Jodar, A. Osuna, F. Rodriguez-Serrano, The role of exosomes on colorectal cancer: a review, J. Gastroenterol. Hepatol. 33 (2018) 792–799.
[3] X. Liang, M. Chen, P. Bhattarai, S. Hameed, Z. Dai, Perfluorocarbon@Porphyrin nanoparticles for tumor hypoxia relief to enhance photodynamic therapy against liver metastasis of colon cancer, ACS Nano 14 (2020) 13569–13583.
[4] M.K. Shim, Y. Moon, S. Yang, J. Kim, H. Cho, S. Lim, H.Y. Yoon, J.K. Seong, K. Kim, Cancer-specific drug-drug nanoparticles of pro-apoptotic and cathepsin B-cleavable peptide-conjugated doxorubicin for drug-resistant cancer therapy, Biomaterials 261 (2020) 120347.
[5] W.B. Strum, Colorectal adenomas, N. Engl. J. Med. 375 (2016) 389–390.
[6] Y. Yao, C. Rao, G. Zheng, S. Wang, Luteolin suppresses colorectal cancer cell metastasis via regulation of the miR-384/pleiotrophin axis, Oncol. Rep. 42 (2019) 131–141.
[7] C.T. Yu, T. Chen, S. Lu, W. Hu, Q. Zhang, J. Tan, D. Sun, L. Li, X. Sun, C. Xu, Y. Lai, M. Fan, Z. Shen, W. Shen, H. Cheng, Identification of significant modules and targets of Xian-Lian-Jie-Du decoction based on the analysis of transcriptomics, proteomics and single-cell transcriptomics in colorectal tumor, J. Inflamm. Res. 15 (2022) 1483–1499.
[8] M. Elmowafy, N.A. Alhakamy, K. Shalaby, S. Alshehri, H.M. Ali, E.F. Mohammed, N.K. Alruwaili, A. Zafar, Hybrid polylactic acid/Eudragit L100 nanoparticles: a promising system for enhancement of bioavailability and pharmacodynamic efficacy of luteolin, J. Drug Deliv. Sci. Technol. 65 (2021) 102727.
[9] P. Shinde, H. Agraval, A. Singh, U.C.S. Yadav, U. Kumar, Synthesis of luteolin loaded zein nanoparticles for targeted cancer therapy improving bioavailability and efficacy, J. Drug Deliv. Sci. Technol. 52 (2019) 369–378.
[10] A.C. McKinlay, R.E. Morris, P. Horcajada, G. Ferey, R. Gref, P. Couvreur, C. Serre, BioMOFs: metal-organic frameworks for biological and medical applications, Angew Chem. Int. Ed. Engl. 49 (2010) 6260–6266.
[11] T.T.T. Nguyen, L.H.T. Nguyen, N.X.D. Mai, H.K.T. Ta, T.L.T. Nguyen, U.-C.N. Le, B.T. Phan, N.N. Doan, T.L.H. Doan, Mild and large-scale synthesis of nanoscale metal-organic framework used as a potential adenine-based drug nanocarrier, J. Drug Deliv. Sci. Technol. 61 (2021) 102135.
[12] R. Karimi Alavijeh, K. Akhbari, Biocompatible MIL-101(Fe) as a smart carrier with high loading potential and sustained release of curcumin, Inorg. Chem. 59 (2020) 3570–3578.
[13] A. Bhattacharjee, S. Gumma, M.K. Purkait, Fe3O4 promoted metal organic framework MIL-100(Fe) for the controlled release of doxorubicin hydrochloride, Microporous Mesoporous Mater. 259 (2018) 203–210.
[14] W. Xie, F. Zhou, X. Li, Z. Liu, M. Zhang, Z. Zong, L. Liang, A surface architectured metal–organic framework for targeting delivery: suppresses cancer growth and metastasis, Arab. J. Chem. 15 (2022) 103672.
[15] B. Singco, L.-H. Liu, Y.-T. Chen, Y.-H. Shih, H.-Y. Huang, C.-H. Lin, Approaches to drug delivery: confinement of aspirin in MIL-100(Fe) and aspirin in the de novo synthesis of metal–organic frameworks, Microporous Mesoporous Mater. 223 (2016) 254–260.
[16] A. Cabrera-Garcia, E. Checa-Chavarria, E. Rivero-Buceta, V. Moreno, E. Fernandez, P. Botella, Amino modified metal-organic frameworks as pH-responsive nanoplatforms for safe delivery of camptothecin, J. Colloid Interface Sci. 541 (2019) 163–174.
[17] N. Pandey, C. Tewari, S. Dhali, B.S. Bohra, S. Rana, S.P.S. Mehta, S. Singhal, A. Chaurasia, N.G. Sahoo, Effect of graphene oxide on the mechanical and thermal properties of graphene oxide/hytrel nanocomposites, J. Thermoplast. Compos. Mater. 34 (2019) 55–67.
[18] X. Li, J.F. Lovell, J. Yoon, X. Chen, Clinical development and potential of photothermal and photodynamic therapies for cancer, Nat. Rev. Clin. Oncol. 17 (2020) 657–674.
[19] Y. Ye, X. Mao, J. Xu, J. Kong, X. Hu, Functional graphene oxide nanocarriers for drug delivery, International Journal of Polymer Science 2019 (2019) 1–7.
[20] R. Abazari, S. Sanati, A. Morsali, Mixed metal Fe2Ni MIL-88B metal–organic frameworks decorated on reduced graphene oxide as a robust and highly efficient electrocatalyst for alkaline water oxidation, Inorg. Chem. 61 (2022) 3396–3405.
[21] A. Ejsmont, A. Lewandowska-Andralojc, K. Hauza, J. Goscianska, In situ modification of Co-MOF with graphene oxide for enhanced photocatalytic hydrogen production, Int. J. Hydrogen Energy 48 (2023) 8965–8970.
[22] Y. Hu, R. Abazari, S. Sanati, M. Nadafan, C.L. Carpenter-Warren, A.M.Z. Slawin, Y. Zhou, A.M. Kirillov, A dual-purpose Ce(III)–Organic framework with amine groups and open metal sites: third-order nonlinear optical activity and catalytic CO2 fixation, ACS Appl. Mater. Interfaces 15 (2023) 37300–37311.
[23] T. Kalhorizadeh, B. Dahrazma, R. Zarghami, S. Mirzababaei, A.M. Kirillov, R. Abazari, Quick removal of metronidazole from aqueous solutions using metal–organic frameworks, New J. Chem. 46 (2022) 9440–9450.
[24] Y. Pan, R. Abazari, J. Yao, J. Gao, Recent progress in 2D metal-organic framework photocatalysts: synthesis, photocatalytic mechanism and applications, J. Phys.: Energy 3 (2021) 032010.
[25] J. Wang, R. Abazari, S. Sanati, A. Ejsmont, J. Goscianska, Y. Zhou, D.P. Dubal, Water-Stable Fluorous Metal–Organic Frameworks with Open Metal Sites and Amine Groups for Efficient Urea Electrocatalytic Oxidation, Small n/a, 2023 2300673.
[26] Y. Cheng, C. Yu, W. Li, Y. He, Y. Bao, Matrine inhibits proliferation, invasion, and migration and induces apoptosis of colorectal cancer cells via miR-10b/PTEN pathway, Cancer Biother. Radiopharm. 37 (2022) 871–881.
[27] A.D.S. Barbosa, D. Julião, D.M. Fernandes, A.F. Peixoto, C. Freire, B. de Castro, C.M. Granadeiro, S.S. Balula, L. Cunha-Silva, Catalytic performance and electrochemical behaviour of Metal–organic frameworks: MIL-101(Fe) versus NH2-MIL-101(Fe), Polyhedron 127 (2017) 464–470.

[28] Y. Sun, Z.-Y. Cheng, J.-Y. Wei, X.-Y. Li, J.-Y. Fang, M.-F. Wang, Preparation and pseudocapacitance performance of Ni-MOF/GO nanomaterial with high specific capacitance, N. Chem. Mater. 51 (2023) 106–112.
[29] Shayesteh Tafazoli, Fatemeh Rafiemanzelat, Farshid Hassanzadeh, M. Rostami, Synthesis and characterization of novel biodegradable water dispersed poly (ether-urethane)s and their MWCNT-AS nanocomposites functionalized with aspartic acid as dispersing agent, Iran. Polym. J. (Engl. Ed.) 27 (2018) 755–774.
[30] H. Liu, T. Xu, C. Cai, K. Liu, W. Liu, M. Zhang, H. Du, C. Si, K. Zhang, Multifunctional superelastic, superhydrophilic, and ultralight nanocellulose-based composite carbon aerogels for compressive supercapacitor and strain sensor, Adv. Funct. Mater. 32 (2022) 2113082.
[31] X. Li, Y. Tang, J. Zhu, H. Lv, L. Zhao, W. Wang, C. Zhi, H. Li, Boosting the cycling stability of aqueous flexible Zn batteries via F doping in nickel-cobalt carbonate hydroxide cathode, Small 16 (2020) e2001935.
[32] T.A. Amollo, G.T. Mola, V.O. Nyamori, Germanium quantum dot/nitrogen-doped graphene nanocomposite for high-performance bulk heterojunction solar cells, RSC Adv. 8 (2018) 21841–21849.
[33] Y. Zhang, Y. Zhang, K. Zhang, K. Jia, G. Liu, X. He, W. Liu, K. Li, Z. Zhang, Nitrogen-Doped graphene nanosheet coated nanospherical Fe3O4 from zeolitic imidazolate frameworks template as anode of lithium ion batteries, Energy Fuels 34 (2020) 14986–14994.
[34] P. Parimal, B. Stuti, R. Pranita, M. Zinia, K. Manoj, T. Vivek, S. Sanjay, P.B. Varsha, Iron oxide nanoparticle encapsulated; folic acid tethered dual metal organic framework-based nanocomposite for MRI and selective targeting of folate receptor expressing breast cancer cells, Microporous Mesoporous Mater. (2022) 112008.
[35] D. Huang, L. Sun, L. Huang, Y. Chen, Nanodrug delivery systems modulate tumor vessels to increase the enhanced permeability and retention effect, J Pers Med 11 (2021).
[36] F. Chen, Y. Pan, J. Xu, B. Liu, H. Song, Research progress of matrine's anticancer activity and its molecular mechanism, J. Ethnopharmacol. 286 (2022) 114914.
[37] K.C. Chen, W.H. Hsu, J.Y. Ho, C.W. Lin, C.Y. Chu, C.C. Kandaswami, M.T. Lee, C.H. Cheng, Flavonoids Luteolin and Quercetin Inhibit RPS19 and contributes to metastasis of cancer cells through c-Myc reduction, J. Food Drug Anal. 26 (2018) 1180–1191.
[38] Y.-C. Lin, L.-C. Liu, C.-T. Ho, C.-M. Hung, T.-D. Way, Luteolin inhibits ER-α expression through ILK inhibition is regulated by a pathway involving Twist and YB-1, J. Funct.Foods 42 (2018) 75–84.
[39] H.U. Rashid, Y. Xu, Y. Muhammad, L. Wang, J. Jiang, Research advances on anticancer activities of matrine and its derivatives: an updated overview, Eur. J. Med. Chem. 161 (2019) 205–238.
[40] X. Meng, X. Zhang, M. Liu, B. Cai, N. He, Z. Wang, Fenton reaction-based nanomedicine in cancer chemodynamic and synergistic therapy, Appl. Mater. Today 21 (2020) 100864.
[41] B. Wang, X. Zhang, Z. Wang, D. Shi, Ferroptotic nanomaterials enhance cancer therapy via boosting Fenton-reaction, J. Drug Deliv. Sci. Technol. 59 (2020) 101883.
[42] T.J. Fan, L.H. Han, R.S. Cong, J. Liang, Caspase family proteases and apoptosis, Acta Biochim. Biophys. Sin. 37 (2005) 719–727.
[43] M. Gryko, M. Lukaszewicz-Zajac, K. Guzinska-Ustymowicz, M. Kucharewicz, B. Mroczko, U. Algirdas, The caspase-8 and procaspase-3 expression in gastric cancer and non-cancer mucosa in relation to clinico-morphological factors and some apoptosis-associated proteins, Adv. Med. Sci. 68 (2023) 94–100.
[44] Y. Qian, C. Shi, C. Cheng, D. Liao, J. Liu, G.-t. Chen, Ginger polysaccharide UGP1 suppressed human colon cancer growth via p53, Bax/Bcl-2, caspase-3 pathways and immunomodulation, Food Sci. Hum. Wellness 12 (2023) 467–476.
[45] M. Velayutham, B. Haridevamuthu, M.F. Elsadek, H. Rizwana, A. Juliet, K.M. Karuppiah, J. Arockiaraj, S-adenosylmethionine synthase-derived GR15 peptide suppresses proliferation of breast cancer cells by upregulating the caspase-mediated apoptotic pathway: in vitro and in silico analyses, J. King Saud Univ. Sci. 34 (2022) 102354.